J Mater Sci (2017) 52:12608–12623

Ceramics

Stress and strain mapping of micro-domain bundles in barium titanate using electron backscatter diffraction

Jane A. Howell[1], Mark D. Vaudin[1], Lawrence H. Friedman[1], and Robert F. Cook[1,*]

[1] *Materials Measurement Science Division, National Institute of Standards and Technology, Gaithersburg, MD 20899, USA*

Received: 17 April 2017
Accepted: 4 July 2017
Published online: 1 August 2017

ABSTRACT

Cross-correlation of electron backscatter diffraction patterns has been used to generate stress and strain maps of a single crystal of tetragonal barium titanate ($BaTiO_3$) containing bundles of small, (0.2–5) μm, *a*- and *c*-domains separated by 90° domain boundaries. The strains peaked at the domain boundaries, and approximately equal, but opposite, values were observed in the *a*- and *c*-domains; the peak strain magnitudes were slightly less than half the tetragonal distortion of $BaTiO_3$, about 0.004, consistent with a tendency to a cubic structure at domain boundaries. The strain state was dominated by two normal strains: in-plane, perpendicular to domain wall intersections with the surface, and out-of-plane, perpendicular to the surface. In distinction to larger, lamellar domains, significant shear strains were also observed. Stress maps were constructed from strain maps using a method that does not require zero stress at reference locations. Peak in-plane normal stresses of approximately 700 MPa were observed. The variation of the stress component parallel to the domain walls was used to determine numerically a microstructurally based stress intensity factor for crack propagation perpendicular to the domain walls. The conditions for stable micro-crack formation in the microstructural stress field and unstable crack propagation under the action of a superposed applied stress were considered in the context of multi-layer ceramic capacitor reliability.

Introduction

Multi-layer ceramic capacitors (MLCCs) [1, 2] are the most frequently used passive component in microelectronic devices. Such capacitors are formed in submillimeter-scale form factors by co-sintering interdigitated layers of a dielectric, usually polycrystalline barium titanate ($BaTiO_3$) ceramic, and conducting metallic electrodes. The small dimensions require modern MLCCs to contain as many as 1000 of these layers, each sub-micrometer in thickness [3]. Driven by increasing demand, over two trillion MLCCs are predicted to be manufactured in 2016 [4]. As a consequence of the large number of MLCCs used, even small deficiencies in MLCC reliability can lead to large numbers of defective devices. In particular, fracture of the brittle ceramic dielectric layers,

Address correspondence to E-mail: robert.cook@nist.gov

DOI 10.1007/s10853-017-1355-4

and consequent failure of an entire MLCC, is a major concern of MLCC manufacturers and assemblers of microelectronic devices. Such fractures can be driven by localized stresses applied to a MLCC during attachment to a circuit board or by global stresses acting almost uniformly over a MLCC during flexure or bending of a circuit board with a MLCC attached [5, 6].

The stresses applied to a MLCC during or after attachment to a circuit board superpose on stresses preexisting in the $BaTiO_3$ microstructure generated by two different mechanisms during the co-sintering process. The first mechanism is related to coefficient of thermal expansion (CTE) inhomogeneity between the ceramic and metal layers. On cooling from sintering, the greater CTE value of the metal electrodes relative to that of the $BaTiO_3$ dielectric leads to compressive stresses in the $BaTiO_3$. These stresses are the order of tens of megapascals in magnitude and vary over length scales set by the millimeter dimensions of the MLCC [7]. As they are small and compressive, these stresses are typically not a ceramic fracture reliability concern.

The second stress generation mechanism is related to the anisotropy of the $BaTiO_3$ crystal structure. At temperatures greater than approximately 120 °C, $BaTiO_3$ is cubic and paraelectric [2, 8]. At temperatures less than this, $BaTiO_3$ undergoes a cubic–tetragonal, and associated paraelectric–ferroelectric, phase transition such that at room temperature in an unstrained state, $BaTiO_3$ has a tetragonal unit cell with the [001] *c*-axis approximately 1.1% longer than the [100] and [010] *a*-axes and ferroelectric polarization parallel to the *c*-axis. During MLCC fabrication, the $BaTiO_3$ initially consists of a porous sheet of randomly oriented single-crystal particles [1, 2]. On sintering, a dense microstructure is generated that thus contains grains and domains (regions of aligned polarization within grains) of different orientations separated by grain and domain boundaries. As a consequence, on cooling $BaTiO_3$ from the sintering temperature (typically greater than 1000 °C [1, 2]) to room temperature, tetragonal distortion mismatches develop between differently oriented grains and domains as the material passes through the cubic–tetragonal phase transition. If strain compatibility is maintained (no cracks, no voids), the mutual constraints of neighboring mis-aligned grains and domains lead to strains and thus reaction stresses. These stresses are maximized at 90° domain boundaries, at which the *c*-axes are perpendicular (and the *c*- and one *a*-axis is colinear) in domains either side of the boundary [9, 10]; the boundary plane can be either {101} or {111}. Recent determinations using electron backscatter diffraction (EBSD) of 90° domain boundary-related stresses in $BaTiO_3$ [11] indicate stresses of hundreds of megapascals varying over length scales of tens of micrometers set by the dimensions of the domains. These stresses are both tensile and compressive and are the major mechanical reliability concern.

Domain boundary-related stresses and strains determined by EBSD are the focus of the work here, extending the previous work [11] in two important ways to approach the domain structures more likely to appear in modern MLCC polycrystalline $BaTiO_3$ dielectric layers [1, 12]: (1) The domains will be *smaller*, micro or nano (a few micrometers to submicrometer) in scale, and (2) the domains will have *more complicated* (fully triaxial) stress and strain states. As context for the current work, Fig. 1a shows a schematic diagram of the simple domain structure studied previously. The sample was a predominantly *c*-domain single crystal, about 4 mm × 3 mm × 1 mm. The domains were long lamellae extending across the 4 mm × 3 mm face and through the 1 mm thickness of the sample; a single *a*-domain imbedded in *c*-domain matrix is shown. As before, "*c*-domain" indicates that [001] is perpendicular to the large face (and parallel to *Z* in the *XYZ* sample coordinate system shown) and "*a*-domain" indicates that [100] or [010] is perpendicular to the large face. Both *a*- and *c*-domains were observed, both about 10 μm in width, separated by 90° {101} domain boundaries inclined at approximately 45° to the sample surface. These are similar to the "laminar twinning" and "parallel stripes" structures described in early observations of $BaTiO_3$ [13, 14].

EBSD patterns were (1) indexed to obtain domain orientations and (2) cross-correlated to obtain components of the strain tensor relative to separate *a*- and *c*-domain reference points within line scans across lamellar structures as shown in Fig. 1a. Components of the stress tensor were determined from the strain components and $BaTiO_3$ elastic constants; the EBSD measurements were assumed to be surface localized such that $\sigma_{zz} = 0$. Figure 2 shows an example of the variation of strain components ε_{xx} and ε_{zz} across the lamellae from near the center of a 100-μm scan [11]; the *a*-domains are indicated by gray shading. For

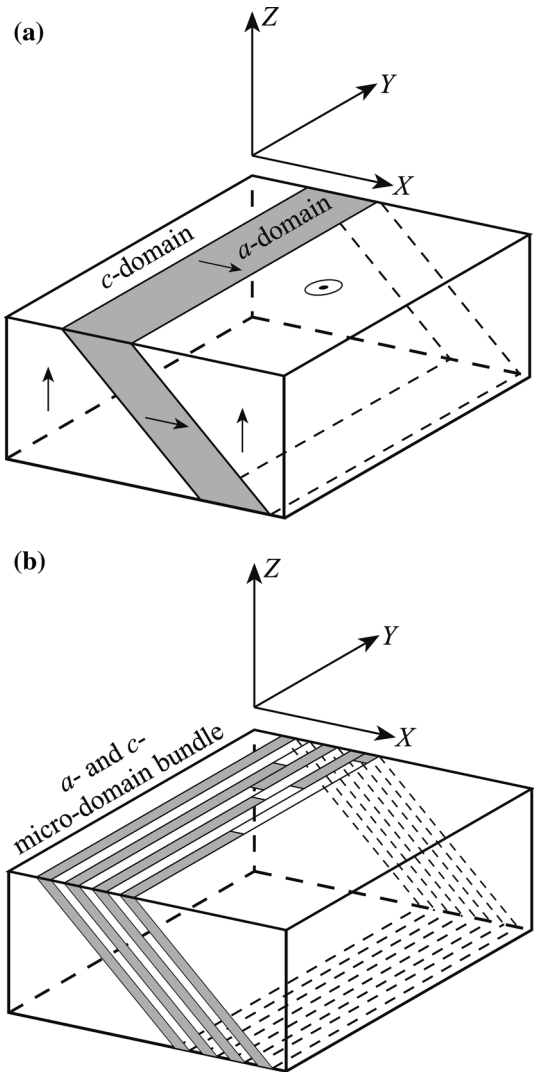

Figure 1 **a** Schematic diagram of a single lamellar *a*-domain (shown *shaded*) in a *c*-domain $BaTiO_3$ crystal. The polarization directions relative to the *XYZ* sample axis are indicated with *arrows*. **b** Schematic diagram of a bundle of alternating *a*- and *c*-domains imbedded in a *c*-domain $BaTiO_3$ crystal. The *shading* and sample axes are shown in (**a**).

both strain components, the strain magnitudes reached maxima as a domain boundary was approached and underwent rapid reversal of sign as the boundary was crossed. The ε_{xx} and ε_{zz} components mirrored each other closely, being of opposite signs with ε_{xx} about 50% relatively greater than ε_{zz}. The variations in the strain components are consistent with crystallographic considerations as the tetragonal unit cell rotates 90° about *Y* at domain boundaries while maintaining strain compatibility. The dark-shaded bands in Fig. 2 indicate the range of the remaining strain components, ε_{yy}, ε_{xy}, ε_{yz}, and ε_{xz} observed over the same lamellae. All were near-negligible suggesting a deformation state of plane strain, $\varepsilon_{yy} = 0$, consistent with long lamellar domains in the *Y*-direction (Fig. 1a), and variations primarily in the normal strains ε_{xx} and ε_{zz}, consistent with strain gradients restricted mostly to the domain boundaries. Similar localization of strain and strain changes at long lamellar *a*–*c* domain boundaries has been observed by reflection electron microscopy and X-ray diffraction [15–18].

The following section contains descriptions of the materials and methods used here to study stress and strain states in micro- and nano-scale domains in $BaTiO_3$. As previously [11], the material is a predominantly *c*-domain single crystal, but in this case containing *a*-domains that are both smaller and more complicated in geometry than the lamellae described above. The experimental methods are similar to those used previously, although more, and more closely spaced, EBSD patterns are used in order to characterize the more complicated strain field. Strain is obtained from EBSD measurements as before, but the stress analysis is extended from that used previously to take into account nonzero stress states at reference points. Strain ellipsoids are introduced to provide simple pictorial representations of strain changes within domains and at domain boundaries. A fracture mechanics analysis is developed to determine crack driving forces from experimental stress measurements. Application of the fracture analysis in assessing MLCC reliability is demonstrated.

Materials and methods

Materials

The sample used for all experiments was a $BaTiO_3$ single crystal grown by the top-seeded solution growth method. The as-received sample was a plate 5 mm × 5 mm × 1 mm, electrically poled such that the majority of the sample was oriented as *c*-domain, but some 90° and 180° domains were still present. The sample as-received was polished on one large face by chemical–mechanical polishing. An additional polishing step of five minutes using colloidal silica was performed on this face. An optical micrograph of part of the face is shown in Fig. 3a: 90° domain features appear as vertical dark or light bands extending across the sample; 180° domains

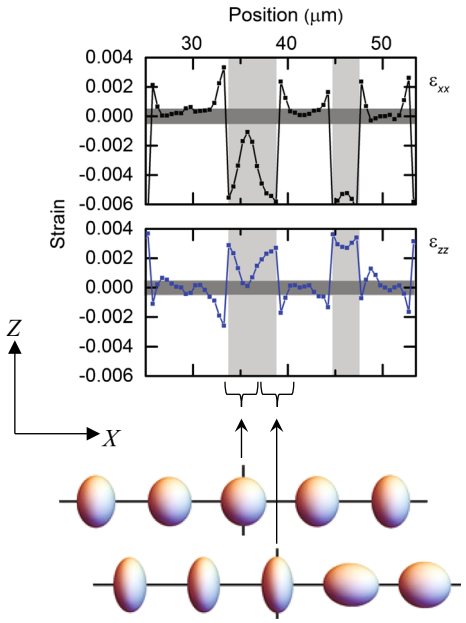

Figure 2 Strain profiles covering several lamellar domains from [11]; the dominant ε_{xx} and ε_{zz} strain components are shown and *a*-domains are *shaded*. Also shown are strain *ellipsoids* from locations 0.5 μm apart centered on an *a*-domain (*upper*) and at the edge of an *a*-domain (*lower*); the strains are magnified 60×. See Online Resource 2 for an animation of these *ellipsoids*.

appear as isolated blocky features similar to the early observations [19, 20]. The dark bands were identified as lamellar *a*-domains, similar to those observed in the previous study [11]. These domains were darker in contrast to the *c*-domain matrix, extended across the sample as straight bands about 10 μm wide, and exhibited negligible change in surface topography relative to the surrounding matrix. These domains and the 180° domains will not be studied here.

The domain-related features studied here were also linear features, but exhibited lighter overall contrast relative to the *c*-domain matrix, extended across the sample as straight bands parallel to *Y* approximately 20–50 μm wide, and exhibited an irregular, roughened surface topography primarily parallel to the long axis of the bands. Such a band is shown in the right side in Fig. 3a and in a higher magnification optical image in Fig. 3b. As will be shown below, the bands consist of many plate-like alternating orientation domains of micrometer or sub-micrometer width and are similar to the "microdomains" [21–24] or "prismatic groups of laminae" described previously [13] and hence will be referred to as micro-domain bundles. A schematic diagram of the micro-domain bundles and the *XYZ* coordinate system used for this sample is shown in Fig. 1b. Most micro-domain bundles were aligned along the *Y*-direction. Several bundles were examined using the orientation and strain analyses described below, and the representative results from a single 45-μm-wide bundle are presented.

Orientation analysis

The orientations of the sample matrix and domains were determined from EBSD patterns (EBSPs) obtained from the sample surface. The surface was not coated prior to loading into a field emission scanning electron microscope (Hitachi S4700 FESEM, Hitachi High Tech, Tokyo, Japan) for EBSD analysis. High-resolution EBSPs were recorded using an accelerating voltage of 20 kV and a beam current of ≈2 nA with the sample tilted 70° about the *X*-axis. Line scans were performed in the *X*-direction to obtain rows of EBSPs. For the case here, each row consisted of 225 EBSPs obtained from points separated in the *X*-direction by 0.2 μm. Full two-dimensional (2-D) maps, 45 μm × 5 μm, were obtained by combining ten such rows separated in the *Y*-direction by 0.5 μm. Each EBSP consisted of an image of 1344 × 1024 pixels; no binning was applied to the EBSPs, which were recorded at high gain with automatic and static background subtraction. Each pattern was collected in approximately 1 s. Each EBSP was indexed to obtain crystal orientation at a scan point using Oxford HKL Flamenco software (version 5.0.9.1, Oxford Instruments, Abingdon, UK). Kikuchi band detection was determined with a resolution of the Hough space of 125, using the band edges from a circular region centered on the middle of the EBSP with a radius of 511 pixels. Indexing was determined from the automatic detection of five to six bands and provided the local orientation of the tetragonal crystal in (1, 2, 3) = (a, a, c) crystal axes relative to the *XYZ* sample axes in terms of microscope Euler angles. A local crystal orientation in the sample was regarded as part of a *c*-domain if the (3, *Z*) angle was close to 0, and as part of an *a*-domain if the (1, *Z*) angle was close to 0. In practice, the (2, *Y*) angle was always close to 0,

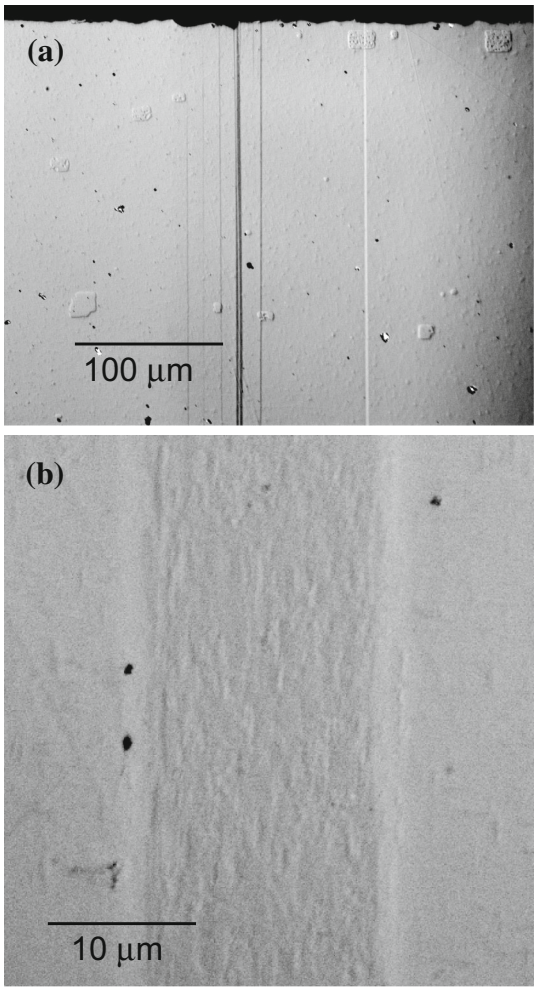

Figure 3 Optical micrographs of the $BaTiO_3$ crystal examined here. **a** Large view of the crystal showing block-like 180° domains and linear lamellar and bundled 90° domains. **b** Magnified view of a micro-domain bundle.

such that the transformation from a *c*-domain to an *a*-domain was accomplished by a ± 90° rotation about *Y*.

Elastic constants

In the crystal axes, the stress and strain tensors are given by σ_{ij} and ε_{ij} ($i, j = 1, 2, 3$), where ε_{ij} does *not* include the tetragonal distortion. In a *c*-domain, the (1, 2, 3) crystal axes transform to the (*X*, *Y*, *Z*) sample axes simply, by (1, 2, 3) → (*X*, *Y*, *Z*). Thus, in contracted Voigt notation the stress and strain vectors σ_K and ε_L in a *c*-domain, specified in the sample frame, are given simply by [25, 26]

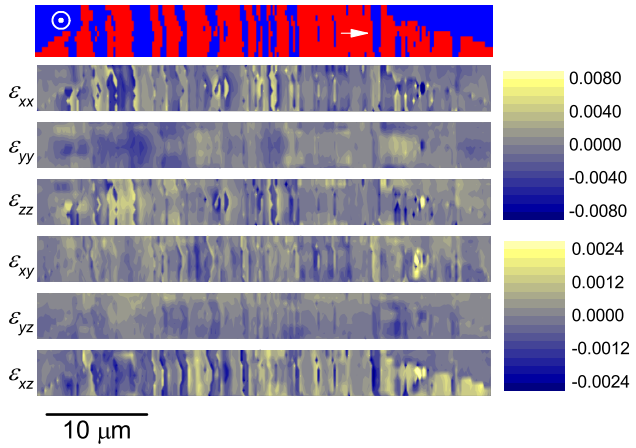

Figure 4 Domain orientation and strain maps across a micro-domain bundle. The scale for the normal strain components is given by the upper scale and for the shear strain components by the lower scale. The locations of the (assigned strain free) reference points are indicated by the *bullseye* and *arrow symbols*.

$$\sigma_K = \begin{bmatrix} \sigma_{xx} \\ \sigma_{yy} \\ \sigma_{zz} \\ \sigma_{yz} \\ \sigma_{xz} \\ \sigma_{xy} \end{bmatrix} = \begin{bmatrix} \sigma_{11} \\ \sigma_{22} \\ \sigma_{33} \\ \sigma_{23} \\ \sigma_{13} \\ \sigma_{12} \end{bmatrix} \text{ and } \varepsilon_L = \begin{bmatrix} \varepsilon_{xx} \\ \varepsilon_{yy} \\ \varepsilon_{zz} \\ \varepsilon_{yz} \\ \varepsilon_{xz} \\ \varepsilon_{xy} \end{bmatrix} = \begin{bmatrix} \varepsilon_{11} \\ \varepsilon_{22} \\ \varepsilon_{33} \\ 2\varepsilon_{23} \\ 2\varepsilon_{13} \\ 2\varepsilon_{12} \end{bmatrix}, \quad c \text{ - domain} \tag{1}$$

where

$$\sigma_K = (C_{KL})_c \varepsilon_L \tag{2}$$

and the indices *K* and *L* range over the sample coordinates as (*xx*, *yy*, *zz*, *yz*, *xz*, *xy*). The elastic stiffness matrix in the sample frame for tetragonal barium titanate $(C_{KL})_c$ is identical to that specified in the crystal frame and is given by [26]

$$(C_{KL})_c = \begin{bmatrix} C_{11} & C_{12} & C_{13} & 0 & 0 & 0 \\ & C_{11} & C_{13} & 0 & 0 & 0 \\ & & C_{33} & 0 & 0 & 0 \\ & & & C_{44} & 0 & 0 \\ & \text{sym.} & & & C_{44} & 0 \\ & & & & & C_{66} \end{bmatrix} = \begin{bmatrix} 275 & 179 & 152 & 0 & 0 & 0 \\ & 275 & 152 & 0 & 0 & 0 \\ & & 165 & 0 & 0 & 0 \\ & & & 54.4 & 0 & 0 \\ & \text{sym.} & & & 54.4 & 0 \\ & & & & & 113 \end{bmatrix} (GPa) \tag{3}$$

where the second equality gives the numerical values [27]. In an *a*-domain, the transformation from the

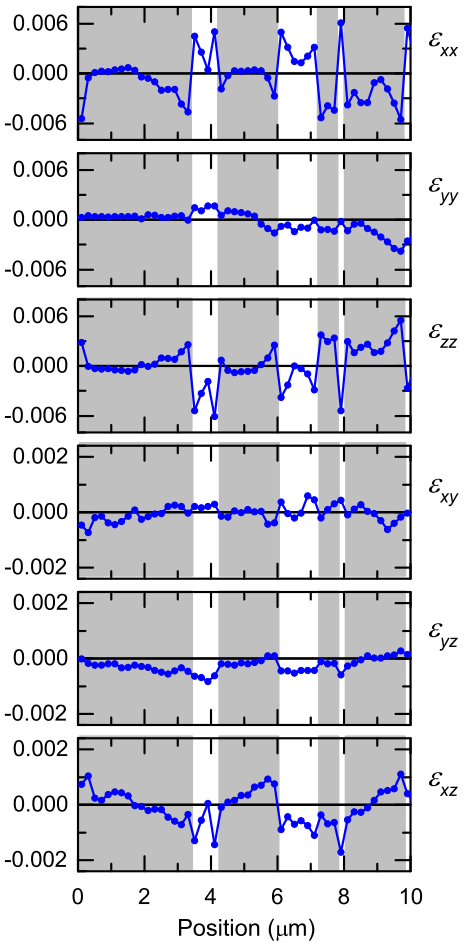

Figure 5 Strain profiles covering several micro-domains taken from the lower left 10 μm of the maps in Fig. 4. The *a*-domains are shown *shaded*. Note that the normal and shear strain scales are different.

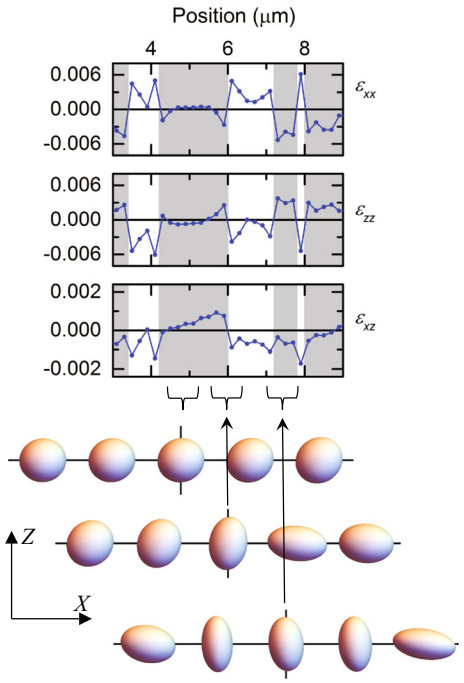

Figure 6 Strain profiles covering the central micro-domains in Fig. 5. The dominant ε_{xx}, ε_{zz}, and ε_{xz} strain components are shown, and *a*-domains are *shaded*. Also shown are strain ellipsoids from locations near the center of a large *a*-domain (*upper*), at the edge of an *a*-domain (*center*), and near the center of a small *a*-domain (*lower*). *Ellipsoids* are drawn with the same scale factor as shown in Fig. 2. See Online Resource 3 for an animation of these *ellipsoids*.

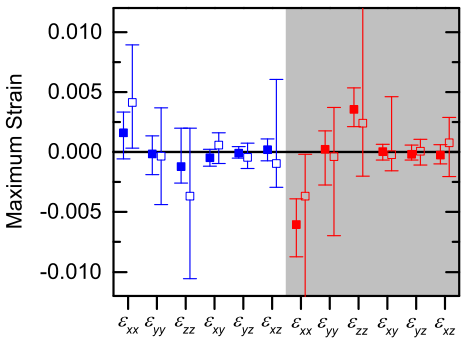

Figure 7 Comparison of the maximum strain distributions in lamellar domains (*solid symbols*) and micro-domains from bundles (*open symbols*). The *bars* represent the ranges observed, and *a*-domain measurements are shown on the *right* against a *shaded* background.

crystal frame to the sample frame is (taking +90° rotation) (1, 2, 3) → (*Z*, *Y*, −*X*). Transforming the stress and strain tensors appropriately [25, 26] and reverting to contracted notation give

$$\sigma_K = \begin{bmatrix} \sigma_{xx} \\ \sigma_{yy} \\ \sigma_{zz} \\ \sigma_{yz} \\ \sigma_{xz} \\ \sigma_{xy} \end{bmatrix} = \begin{bmatrix} \sigma_{33} \\ \sigma_{22} \\ \sigma_{11} \\ -\sigma_{12} \\ -\sigma_{13} \\ \sigma_{23} \end{bmatrix} \text{ and } \varepsilon_K = \begin{bmatrix} \varepsilon_{xx} \\ \varepsilon_{yy} \\ \varepsilon_{zz} \\ \varepsilon_{yz} \\ \varepsilon_{xz} \\ \varepsilon_{xy} \end{bmatrix} = \begin{bmatrix} \varepsilon_{33} \\ \varepsilon_{22} \\ \varepsilon_{11} \\ -2\varepsilon_{12} \\ -2\varepsilon_{13} \\ 2\varepsilon_{23} \end{bmatrix}, \quad (4)$$

a - domain

where

$$\sigma_K = (C_{KL})_a \varepsilon_L \quad (5)$$

and the indices are specified as above. The elastic stiffness matrix in the sample frame relating the stress and strain vectors is now given by

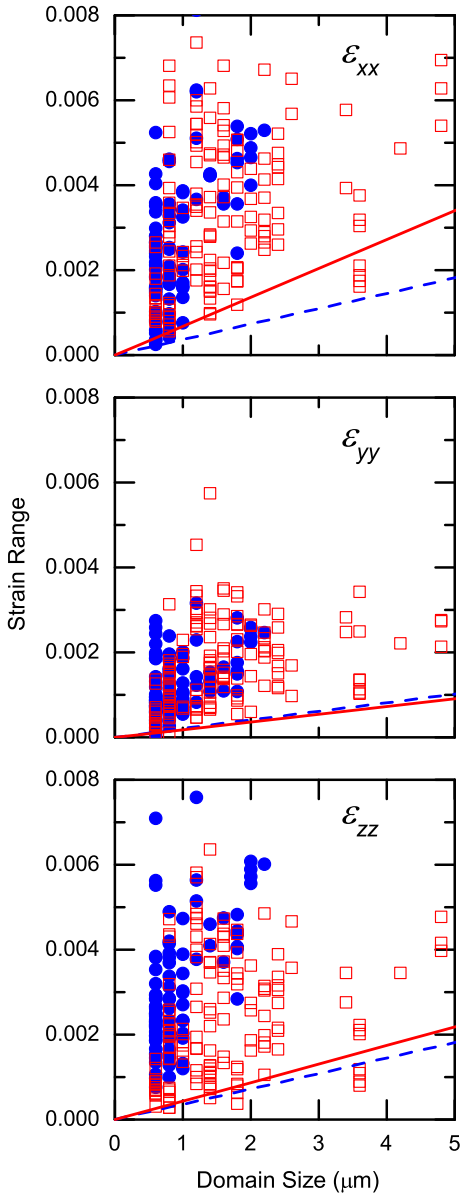

Figure 8 Plots of maximum ε_{xx}, ε_{zz}, and ε_{xz} strain components as a function of domain size (width) for micro-domains; *c*-domains *solid symbols*, *a*-domains *open symbols*. *Solid* and *dashed lines* represent the extrapolated responses for larger lamellar *a*-domains and *c*-domains, respectively.

$$(C_{KL})_a = \begin{bmatrix} C_{33} & C_{13} & C_{13} & 0 & 0 & 0 \\ & C_{11} & C_{12} & 0 & 0 & 0 \\ & & C_{11} & 0 & 0 & 0 \\ & & & C_{66} & 0 & 0 \\ & \text{sym.} & & & C_{44} & 0 \\ & & & & & C_{44} \end{bmatrix} \quad (6)$$

The C_{KL} matrices given above will be used below in two ways: first, in a limited manner to obtain the full strain tensor from EBSD measurements, and second, to obtain the full stress tensor from the full strain tensor.

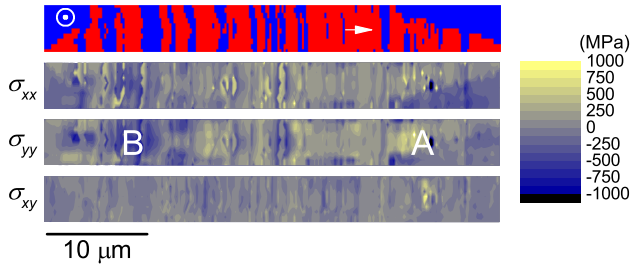

Figure 9 Domain orientation and stress maps across a micro-domain bundle (same area as Fig. 4). The locations of the (assigned strain free) reference points are indicated by the *bullseye* and *arrow symbols*.

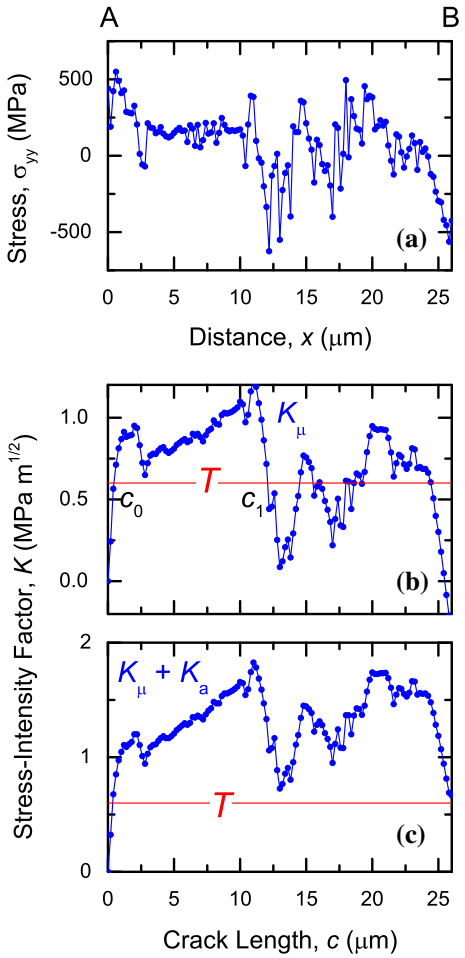

Figure 10 **a** Plot of the variation in the σ_{yy} stress component between locations A and B in Fig. 9. **b** Plot of the SIF K_μ arising from the stress variation in the upper plot. **c** Plot of the summed SIF $K_\mu + K_a$ when a uniform applied stress is superposed on the stress variation in the upper plot.

Strain analysis

An entire map (2250 EBSPs) was analyzed for strain using the method of cross-correlation (CrossCourt 3.0, BLG Productions, Bristol, UK). Two reference patterns were used in each dataset: one in the center of a *c*-domain and one in the center of an *a*-domain (domains were determined from the orientation analysis). All *c*-domains were analyzed with the *c*-domain reference, and all *a*-domains were analyzed with the *a*-domain reference. Reference patterns were assigned (by definition) zero strain; all strains are thus relative to these points. The eight independent components of the local traceless distortion tensor, $\tilde{A}_{ij}$, in the crystal coordinates ($i, j = 1, 2, 3$) were determined at each location from analysis of 20 regions of interest (256 × 256 pixels) from each EBSP [28]. The off-diagonal components of $\tilde{A}_{ij}$ are identical to those of the full nine-component distortion tensor, A_{ij}, *e.g.*, $\tilde{A}_{12} = A_{12}$, but only two of the diagonal terms of $\tilde{A}_{ij}$ are determined and are expressed in terms of diagonal components of the full distortion tensor by $\tilde{A}_{11} = (A_{11} - A_{33})$ and $\tilde{A}_{22} = (A_{22} - A_{33})$. The local infinitesimal strain tensor is related to the full distortion tensor by $\varepsilon_{ij} = (A_{ij} + A_{ji})/2$ [25, 26], noting that for $i = j$ the normal strains are identical to the diagonal components of the full distortion tensor, such that, *e.g.*, $\varepsilon_{11} = A_{11}$, and thus, $\varepsilon_{11} = (\tilde{A}_{11} + \varepsilon_{33})$. To obtain (or close) the full distortion tensor and obtain the strain tensor, the surface with normal Z is taken as in traction-free equilibrium such that in the sample coordinate system $\sigma_{zz} = 0$ at all locations. Using these relations and Eqs. 1 to 6, separate expressions for ε_{33} for each domain type in crystal coordinates are obtained:

$$\varepsilon_{33} = -\frac{C_{13}(\tilde{A}_{11} + \tilde{A}_{22})}{(2C_{13} + C_{33})} \quad c\text{ - domain} \tag{7}$$

$$\varepsilon_{33} = -\frac{(C_{11}\tilde{A}_{11} + C_{12}\tilde{A}_{22})}{(C_{11} + C_{12} + C_{13})} \quad a\text{ - domain} \tag{8}$$

The full strain tensor in the crystal axes is thus easily obtained and transformed to the sample axes by Eqs. 1 or 4.

The strain tensor may be represented by a strain ellipsoid, given by [26]

$$\frac{x_{\mathrm{I}}^2}{(1+\varepsilon_{\mathrm{I}})^2} + \frac{x_{\mathrm{II}}^2}{(1+\varepsilon_{\mathrm{II}})^2} + \frac{x_{\mathrm{III}}^2}{(1+\varepsilon_{\mathrm{III}})^2} = 1 \tag{9}$$

where ε_{I}, $\varepsilon_{\mathrm{II}}$, and $\varepsilon_{\mathrm{III}}$ are the local principal strains of the strain tensor in sample coordinates and x_{I}, x_{II}, and x_{III} are coordinates in the conjugate local principal directions. The size, shape, and orientation of the strain ellipsoid indicate the deformation a unit sphere of material has undergone at that location. Representations of strain ellipsoids were determined by solving the tensor equation $\boldsymbol{x} \cdot (\mathbf{I} + \boldsymbol{\varepsilon})^{-2} \cdot \boldsymbol{x} = 1$ at each location (Mathematica, Wolfram, Champaign, IL), where $\boldsymbol{x}$ is a vector in XYZ sample coordinates, $\mathbf{I}$ is the identity matrix, and $\boldsymbol{\varepsilon}$ is the complete strain tensor also in sample coordinates. This method is mathematically equivalent to determining the eigenvalues (principal strains, $\varepsilon_{\mathrm{I}}, \varepsilon_{\mathrm{II}}, \varepsilon_{\mathrm{III}}$) and eigenvectors (principal directions, $\boldsymbol{u}_{\mathrm{I}}, \boldsymbol{u}_{\mathrm{II}}, \boldsymbol{u}_{\mathrm{III}}$) of the strain tensor at each location but computationally more efficient.

Stress analysis

By definition, all components of the strain tensor are zero at the reference points, and thus, using Eqs. 2 and 5, all the stress tensor components are mathematically zero at the reference points as well. In previous works, the selection of reference point locations was such that the stresses at the reference point were likely to be zero, and, in fact, this likely stress state was the predominant criterion for selecting reference point locations. Examples include locations remote from wedge indentations [29–31], remote from SiGe overlayers [32, 33], and remote from domain boundaries [11]. No such location was readily available in the bundled domain measurements here, and the reference locations were simply taken in domains with no assurance that the stresses at those locations were in fact zero. However, global mechanical equilibrium requires that each component of the stress tensor averages separately to zero [25]. That is,

$$\langle \sigma_K \rangle = 0 \tag{10}$$

where $\langle\ \rangle$ indicates an average over all locations and K is taken separately for each stress component (and thus Eq. 10 represents six separate equations). Stress was thus evaluated from strain at each location by extending Eqs. 2 and 5 to

$$\sigma_K = (C_{KL})_c \varepsilon_L - (\sigma_K^0)_c \tag{11}$$

$$\sigma_K = (C_{KL})_a \varepsilon_L - (\sigma_K^0)_a \tag{12}$$

The (ten) quantities $(\sigma_K^0)_a$ and $(\sigma_K^0)_c$ evaluated were such that the equilibrium conditions (Eq. 10) were met separately for each domain type (those for σ_{zz} were automatically fulfilled). In practice, this was achieved by determining the stress tensor using the un-modified equations above, calculating the mean stress for each component thus determined and subtracting this mean from each component. The physical meaning of $(\sigma_K^0)_a$ and $(\sigma_K^0)_c$ is that they are the stress components at the reference locations.

Fracture analysis

The spatial variation of stress in the domain microstructure was used to calculate the driving force for crack propagation in the ceramic arising from the constrained phase transformation strains. The crack driving force was calculated using a microstructurally based stress intensity factor (SIF), K_μ. It is demonstrated how calculating K_μ as a function of crack length c can be used in examples of assessing MLCC mechanical reliability.

The fracture evolution of a small, sub-micrometer, crack nucleus located in a region of large tensile stress is modeled. The microstructural stress gives rise to a SIF field, $K_\mu(c)$, that drives crack extension from such a nucleus. If the crack nucleus is of length such that the condition $K_\mu(c) = T$, where T is the toughness of the material, the nucleus will be in a state of unstable equilibrium as $\mathrm{d}K_\mu(c)/\mathrm{d}c > 0$ at small crack lengths in a tensile stress field. Any positive perturbation in nucleus sizes leads to the condition $K_\mu > T$ and the crack will initiate and then grow if the condition $K_\mu > T$ is maintained.

The SIF driving the growth of a potential straight crack of length c propagating in the x direction can be calculated from the stress field prior to cracking using the formula [34]

$$K_\mu(c) = 2(c/\pi)^{1/2} \int_0^c \left[\sigma(x)/\left(c^2 - x^2\right)^{1/2}\right] \mathrm{d}x, \qquad (13)$$

where $\sigma(x)$ is the stress distribution acting over the crack. Here the discrete $\sigma_{yy}(x)$ stress variation will be taken for $\sigma(x)$ (such that a mode-I SIF will be calculated) and the integral will be calculated numerically. For slowly varying stress fields, the integral can be calculated using trapezoidal numerical integration methods, as in the case of CTE-driven stress fields in a recent stress mapping study of polycrystalline alumina [35]. For the rapidly varying stress fields, here a stronger method based on quadrature was used. The method is based on the result from integration of Eq. 13 that a linearly varying stress field, of the form $\sigma(x) = a + bx$, acting over a region $[x_1, x_2]$ on a crack, such that $x_1 < x_2 < c$, $\sigma_1 = \sigma(x_1)$, and $\sigma_2 = \sigma(x_2)$, gives a contribution $\Delta K_\mu(c)$ to the total SIF of

$$\Delta K_\mu(c) = 2\left(\frac{c}{\pi}\right)^{1/2} a\left[\sin^{-1}\left(\frac{x_2}{c}\right) - \sin^{-1}\left(\frac{x_1}{c}\right)\right] - 2\left(\frac{c}{\pi}\right)^{1/2} b\left[\left(c^2 - x_2^2\right)^{1/2} - \left(c^2 - x_1^2\right)^{1/2}\right] \qquad (14)$$

where $a = (\sigma_1 x_2 - \sigma_2 x_1)/(x_2 - x_1)$ and $b = (\sigma_2 - \sigma_1)/(x_2 - x_1)$. The numerical integration procedure to determine the full $K_\mu(c)$ from contributions of many $\Delta K_\mu(c)$ terms was to: (1) select a line scan of discrete measurements $\sigma(x_i)$ from the stress map, where i is a position index, and identify a starting location, $i = 0$, and direction of propagation for a crack along this line; (2) select a crack length, c with final index n; (3) calculate the contributions to the stress intensity factor using Eq. 14, letting i vary from 0 to $n - 1$, such that the indices 1 and 2 in Eq. 14 become i and $i + 1$, and sum the contributions to obtain the full SIF at that crack length; and finally (4) repeat steps (2) and (3) for different crack lengths to obtain the function $K_\mu(c)$. The accuracy of the numerical procedure was validated by comparisons with SIFs of known analytical solutions.

The SIF, K_a, arising from a uniformly applied stress, σ_a, on a crack is given by [34]

$$K_\mathrm{a} = \pi^{1/2}\sigma_\mathrm{a} c^{1/2}. \qquad (15)$$

A net SIF on the crack, K, can be created by using $K = K_\mu$ alone, to represent the effects of the microstructure on spontaneous micro-cracks in the ceramic, or the sum $K = K_\mu + K_\mathrm{a}$, to represent the effect of superposed applied stress, say from flexure of a circuit board [6], on a preexisting microstructurally driven crack.

Results

Strain variation

The domain bundles exhibited more complex strain variation than the lamellar domains discussed in [11]. To illustrate this added complexity, Fig. 2 includes

two sets of strain ellipsoids calculated for the lamellar domains. The ellipsoids are viewed in the *X*–*Z* plane, and strains have been magnified 60 times for easy visualization. (As the ε_{yy} strains for this structure were negligible, this view shows all the important information.) The central ellipsoid in each set was determined at the location indicated by the arrowed line, in the upper set at the center of an *a*-domain and in the lower set at the edge of an *a*-domain adjacent to a domain boundary. The ellipsoids either side of the central ellipsoid are ± 0.5 and ± 1 μm from the center, and the range is indicated by braces. In the upper set, the central ellipsoid is near spherical, consistent with a state of near-zero strain at the center of a domain. Either side of this, the ellipsoids become slightly extended vertically and contracted horizontally as ε_{zz} becomes positive and ε_{xx} becomes negative on moving away from the center of the domain. In contrast, for the lower set, the central ellipsoid and the two to the left are clearly extended vertically and contracted horizontally, indicative of extremely positive ε_{zz} and extremely negative ε_{xx} at the *a*-domain edge. The right two ellipsoids in the lower set are contracted vertically and extended horizontally, reflecting a rapid change in sign of both strain components on crossing the domain boundary into the *c*-domain. The ellipsoids provide a clear pictorial representation of the very small strains at the domain centers and the large strains and changes in principal strain magnitudes at the domain boundaries. The ellipsoids also indicate that the orientations of principal strain directions do not alter much in the structures; the ellipsoid axes $\boldsymbol{u}_{\mathrm{I}}$ and $\boldsymbol{u}_{\mathrm{III}}$ are not rotated discernibly from *X* or *Z*, consistent with insignificant shear strains. Online Resource 1 contains a description of animations of the variation in strain ellipsoids with location in complete scans across the lamellar and micro-domain bundle structures. Online Resource 2 contains the animation for the lamellar structure, which demonstrates that the observations in Fig. 2 are representative.

In contrast, Fig. 4 shows orientation and strain maps for the micro-domain bundle that are more complicated than the maps from lamellar domains. The upper map depicts orientation, with *a*-domains indicated in red and *c*-domains indicated in blue (a color scheme to be used throughout). The locations of the reference points are indicated by the bullseye (*c*-domain) and arrow (*a*-domain) symbols. About 25 domains of each type are apparent, ranging in size from the pixel spacing (0.2 μm) to about 5 μm, with irregular edges aligned approximately along the *Y*-direction. Increasing fraction of the *c*-domain matrix is visible at the bundle edges. The lower six maps are color-fill contour maps of the strain components over the same region. Note that the normal strain components color scale strain range is greater than that of the shear strain components by just over a factor of three. In all component cases, the variation of the strain mostly follows the domain orientation, but includes variations at length scales smaller than the domains, primarily in the *X*-direction, but also in the *Y*-direction. Not only is the strain pattern more complicated than that of the lamellae, it has weaker correlation with the domain orientation [11]. Similar to the lamellar domains, the strain field is dominated by the ε_{xx} and ε_{zz} normal strain components, which exhibit the greatest strain values and strain variability. Dissimilar to the lamellar domains, however, are the magnitudes of the shear strains, which for these bundled domains are significant, especially ε_{xz}, and only a factor of three smaller than the normal strains compared with more than a factor of ten for the lamellar domains.

Figure 5 shows the variation in each of the strain components for the lowest line scan from the left 10 μm of each map from Fig. 4. As before, *a*-domains are indicated by gray shading, and the correlation between strain variation and domain orientation, particularly for ε_{xx}, ε_{zz}, and ε_{xz} is apparent. Also apparent is the strong negative correlation between ε_{xx} and ε_{zz}, especially in the *c*-domains. Comparison with Fig. 2 shows that the signs of strain variation in the bundled domains for ε_{xx} and ε_{zz} are the same as those for the lamellar domains: ε_{xx} is compressive in *a*-domains and tensile in *c*-domains; ε_{zz} is compressive in *c*-domains and tensile in *a*-domains. This observation is consistent with crystallographic and strain compatibility considerations, as noted in Introduction. Comparison with Fig. 2 also shows that both the lamellar and bundled domains exhibit the same spatial variation in strain magnitude with small strains at the centers of domains that increase as the domain boundary is approached before reversing sign at the boundary. The magnitudes of the dominant strain components differ slightly between the two structures, however, as the lamellar domains exhibited the greatest strains in the *a*-domains and

the bundled domains exhibit the greatest strains in the *c*-domains.

Figure 6 shows strain variations and three sets of strain ellipsoids for the micro-domain bundles. The visualization conditions are identical to those for the lamellar domains with the exception that the ellipsoids either side of the central ellipsoid are ± 0.2 μm and ± 0.4 μm from the center. The upper and lower sets of ellipsoids in Fig. 6 are in the center of *a*-domains, and the middle set is at the edge of an *a*-domain adjacent to a domain boundary. The upper set of ellipsoids in Fig. 6 closely resembles the upper set of ellipsoids in Fig. 2: a nearly spherical central ellipsoid reflecting near-zero strain conditions at the center of a large domain, with slight elongation of the ellipsoids on moving away from the domain center. Close inspection suggests the elongation is along the diagonal between *X* and *Z*, consistent with significant shear strain in the domain. The central set of ellipsoids are centered on the *a*-domain edge and, as in the lower set in Fig. 2, the central ellipsoid is extended vertically and contracted horizontally, indicative of large positive ε_{zz} and negative ε_{xx}, but in this case $\boldsymbol{u}_1$ is tilted to the diagonal between *X* and *Z*, indicative of the large positive ε_{xz}. Also as in the lower set in Fig. 2, the right two ellipsoids in the middle set in Fig. 6 are contracted vertically and extended horizontally, reflecting the rapid changes in sign of both the normal strain components on crossing the domain boundary. In this case, the additional change in sign of the significant shear strain is now reflected in the reversal in tilt of the ellipsoids to between the -*X* and *Z* axes. The lower set of ellipsoids in Fig. 6 are centered in a small *a*-domain, in which the strain does not decay to near zero at the domain center, similar to observations in lamellar domains as a function of domain size [11]. The strain state is reflected in the vertical extension, horizontal contraction, and slight negative tilt of $\boldsymbol{u}_1$ of the three central ellipsoids indicating large positive ε_{zz}, large negative ε_{xx}, and moderate negative ε_{xz}. The two outer ellipsoids are reversed in aspect ratio but not tilt, indicative of the large normal strain reversals on crossing the domain boundary with slight increases in shear strain magnitude. Online Resource 3 contains an animation for the micro-domain bundle structure, which demonstrates that the observations in Fig. 6 are representative.

Strain maxima and ranges

Figures 2, 4, 5, and 6 illustrate that there are both similarities and differences in strain variations, and their connection to domain boundaries, between the larger, geometrically simple lamellar domain structure and the smaller, more complicated micro-domain bundle structure. Figure 7 illustrates both the similarities and a difference in a plot of the maximum strain observed in a domain for each strain component. Data for the lamellar domains and bundle domains are indicated by solid and open symbols, respectively; *a*-domain data are shown with a shaded background. Data for the lamellar domains were taken from [11], and those for the bundle domains were taken from measurements of the bundle described here and two others. The similarities are that (1) in both *c*- and *a*-domains the normal strain ε_{yy} and all the shear strains fluctuate in a very narrow band around 0, and (2) in *c*-domains ε_{xx} is predominantly positive and ε_{zz} is predominantly negative and the reverse is true in *a*-domains. The difference is that the dispersion in all the normal strains and to a lesser extent all the shear strains is much greater in the micro-domain bundles than the lamellae, including significant differences in sign from the mean values. The similarities suggest that to first approximation both structures are in a state of plane strain in the *XZ* plane and that strain compatibility is accommodated by both domain types losing tetragonality and becoming more cubic adjacent to domain boundaries with fixed orientation of unit cell axes. The difference suggests that the plane-strain and fixed axes orientation conditions are less well obeyed locally for the micro-domain bundles. The more complicated structure requires a greater diversity of strain states, including significant shear, to maintain compatibility.

Another difference between the lamellae and the bundles is illustrated in Fig. 8, which shows plots of the normal strain ranges observed in each domain as a function of domain size. For the lamellae [11], linear relations, albeit with some scatter, were observed between strain range and domain size over size ranges of 1 μm to 15 μm; these linear relations are shown as the solid (*c*-domains) and dashed (*a*-domains) lines in Fig. 8. The symbols in Fig. 8 represent measurements for individual domains in the three bundles above. No trend with domain size or type is readily discernible, although the observations for the lamellar domains appear to be lower

bounds. The linear trend for the lamellar domains was interpreted [11] as a similar strain gradient in the lamellae adjacent to domain boundaries, suggesting a similar change in unit cell conformation on moving away from boundaries. The lack of real trend observed here suggests a much more complicated and diverse set of changes in unit cell conformation adjacent to domain boundaries in the bundles, consistent with the greater dispersion of strain ranges observed in Fig. 7.

Stress and fracture

Figure 9 shows orientation and stress maps for the micro-domain bundle considered here. The upper map depicts orientation as shown in Fig. 4. The lower three maps are color-fill contour maps of stress components over the same region, calculated from the strains in Fig. 4 and Eqs. 11 and 12. Compared with strain, the variation of stress is more smeared out and more weakly follows the domain orientation, but still includes variations at length scales smaller than the domains. The stress pattern is far more complicated than that of the lamellar domains [11], which exhibited strong correlation between stress and domain orientation. Similar to the lamellar domains, the stress field is dominated by the σ_{xx} and σ_{yy} normal stress components, which exhibited the greatest stress values, of order many hundreds of megapascals, and stress variability. Also similar to the lamellar domains, the magnitude of the in-surface shear stress, σ_{xy}, was much less, reaching just over a hundred megapascals. The mean value of these three stress components was of course 0 due to the imposed global equilibrium condition, Eq. 10, and that for σ_{zz} also 0 due to the imposed traction-free surface condition. The mean value of the remaining, out-of-plane shear stress components, σ_{xz} and σ_{yz}, was also 0 due to the imposed global equilibrium condition, but these components required minimal adjustments of only tens of megapascals, as the experimental measurements already reflected the traction-free state of the surface and any nonzero values are attributed to measurement error.

Figure 10a shows the variation of stress σ_{yy} along the line from locations A to B marked in the stress map in Fig. 9. Location A represents a region of large tensile σ_{yy} in the structure and would thus be a likely location for crack initiation. Location B represents a region of large compressive σ_{yy}; the stress fluctuates considerably as a function of position x between the two locations. Figure 10b shows the variation of the microstructurally based SIF K_μ as a function of crack length c for a crack propagating from A to B. $K_\mu(c)$ was determined from $\sigma_{yy}(x)$ given in Fig. 10a and numerical evaluation of Eq. 13. Figure 10c shows the variation of the sum of $K_\mu + K_a$ with K_μ taken from Fig. 10b and $K_a(c)$ evaluated from Eq. 15 using $\sigma_a = 100$ MPa, a value representative of stresses applied to a MLCC during flexure of a circuit board [6]. Also shown in Fig. 10b and c are horizontal lines representing the toughness, $T \approx 0.6$ MPa $m^{1/2}$ of single-crystal $BaTiO_3$. This value is a lower bound to measurements on polycrystalline $BaTiO_3$ [36–38].

Examination of the relative values of K and T as a function of hypothetical crack length from Fig. 10b and c enables reliability predictions to be made for fracture within a MLCC. As discussed above, as multi-domain $BaTiO_3$ cools below the cubic–tetragonal transformation temperature, stress fields develop throughout the material as shown in Fig. 9. A small, sub-micrometer crack nucleus located at A in Fig. 9 would experience a $K_\mu(c)$ field extending up to and through point B as shown in Fig. 10b. At the extreme left in Fig. 10b, $K_\mu(c_0) = T$ and the nucleus is in a state of unstable equilibrium. The equilibrium is unstable as $dK/dc > 0$ at this crack dimension and any positive perturbation in nucleus size leads to the condition $K > T$ and a crack thus initiates and grows. The crack then follows a nonequilibrium path along $K_\mu(c)$ until the equilibrium condition $K = T$ is again met, at a crack length of about $c_1 = 12.5$ μm near the center in Fig. 10b. At this crack length the equilibrium is stable as here $dK/dc < 0$ and any positive or negative perturbation in crack length leads to a crack driving force to restore the crack to the equilibrium length. Hence, a spontaneous micro-crack driven by the tetragonal mismatch field has "popped-in" and arrested. Such micro-cracks also form in polycrystalline alumina, driven by CTE anisotropy mismatch fields [39].

If the material containing the micro-crack as discussed above is subsequently exposed to a uniformly applied stress of 100 MPa, the combined $K(c)$ field is shown in Fig. 10c. No equilibrium configuration now exists between A and B and $K > T$ over the entire interval. The imposition of the applied stress leads to a stable-to-unstable transition for the arrested 12.5 μm micro-crack, followed by nonequilibrium

extension of the crack. If such extension is unconstrained, the crack passes through the entire material; if contained within a MLCC, the MLCC would be fractured completely into two pieces.

Discussion

The strain measurements here on $BaTiO_3$ micro-domain bundles are broadly consistent with previous measurements on large lamellar $BaTiO_3$ domains (Fig. 7): As a 90° domain boundary is approached, the lattice becomes less tetragonal. In *c*-domains, there is expansion of the *a*-axis in the *x*-direction and contraction of the *c*-axis in the *z*-direction, and in *a*-domains there is contraction of the *c*-axis in the *x*-direction and expansion of the *a*-axis in the *z*-direction. X-ray topography measurements [40] are also consistent with these observations and show that the boundary regions between 90° domains exhibited lattice parameters that were strained and intermediate to those of the tetragonal *a*- and *c*-axes. A limit on the reduction in tetragonality is reached if the lattice becomes cubic at the boundary (ignoring any shear that may be present) such that the upper limit to the normal strains is half the tetragonal distortion. This leads to maximum strain estimates for the domain boundary: $\varepsilon_{xx}(c\text{-domain}) = \varepsilon_{zz}(a\text{-domain}) = 0.0055$ and $\varepsilon_{zz}(c\text{-domain}) = \varepsilon_{xx}(a\text{-domain}) = -0.0055$. The observed maximum values are in good agreement with these upper bounds. From Fig. 7, the mean values are $\varepsilon_{xx}(c\text{-domain}) = 0.0041$, $\varepsilon_{zz}(a\text{-domain}) = 0.0025$, $\varepsilon_{zz}(c\text{-domain}) = -0.0037$, and $\varepsilon_{xx}(a\text{-domain}) = -0.0037$, although as noted there was considerable dispersion in these strain values for the micro-domain bundles. The advantage of the 2-D mapping (Fig. 4) is that such dispersion becomes apparent, a finding that is difficult to establish in X-ray diffraction or transmission electron microscopy studies that examine far fewer boundaries [15–18, 40].

The micro-domain bundles are not just smaller or narrower versions of the lamellar domains. There are considerable differences: The micro-domains exhibited significant shear strain, particularly ε_{xz}, whereas the lamellar domains did not; as noted above, the bundles exhibited significantly greater dispersion in strain than the lamellae; the bundles exhibited no clear trend of strain range with domain size, whereas the lamellae exhibited a near-linear dependence; and, the bundles exhibited a much weaker dependence of strain and stress variation with location relative to domain boundaries. These differences most likely originate from the fact that the domains in the bundles do not extend very far in the *Y*-direction, along the bundle length, thus removing the almost plane-strain constraint exhibited by the lamellae (which would result in zero shear strains [25, 26, 31]). It is also possible that the domains in the bundles do not extend through the sample as shown in Fig. 1b, but instead are also limited in dimension into the sample such that the bundle microstructure consists of a series of microscale platelet domains. Such a microstructure would lead to tetragonal mismatch in all three directions, further complicating the strain field, and would be consistent with the significant shear strains observed in Fig. 4. The lack of order in the micro-domain bundles also distinguishes them from the ordered "herringbone" [9, 14, 19, 23, 24] and "wedge" [22, 23] domain structures that form at similar small length scales in $BaTiO_3$.

Although much more difficult to quantify, the characteristic length scale for strain variation in the micro-domain bundles was much shorter than that exhibited by the lamellae: about 0.4 μm to 0.6 μm for both *a*- and *c*-domains in the bundles compared with 1 μm to 2 μm for *c*-domains and 3 μm to 4 μm for *a*-domains in the lamellae. However, in both domain types, this strained transition region was much larger than the domain wall width, which for $BaTiO_3$ has been has been determined to be a few nanometers [41, 42].

The development of the strain and stress maps here has focused on their use in improving the mechanical reliability of MLCCs, in particular in predicting the conditions under which the $BaTiO_3$ ceramic would fracture. An example of the fracture application is given in Fig. 10, which considers both a stable crack generated in the structure under the sole influence of the microstructurally generated stresses and an unstable crack driven by a superposed applied stress. A single prediction of stable micro-crack length as shown in Fig. 10b can be used in reliability predictions for MLCCs if the stress map in Fig. 9 is developed at a crack-sensitive location within the MLCC, say at the edge [7]. Alternatively, many initial crack nucleus locations and potential crack propagation directions can be selected in a stress map as shown in Fig. 9, to generate many SIF variations as shown in Fig. 10b. The distributions of micro-crack lengths and orientations within a structure can thus be obtained

and the degradation of a property, say elastic modulus [39], for the ceramic in the mapped region of the MLCC can be predicted. If the MLCC was indeed subsequently stressed by the imposed bending of an attached circuit board, predictions of the $K_{\mu}(c)$ field in Fig. 10b can be used in concert with the knowledge of $K_{a}(c)$ to ensure component reliability. In this case, reliability could be assured by placing an upper bound on the bending of the circuit board such that the unconstrained nonequilibrium fracture in Fig. 10c does not occur.

The development of the strain and stress maps could also be used in understanding and improving the *electrical* properties of $BaTiO_3$ and other ferroelectrics. As noted in a review of thin-film ferroelectric oxides [43], many such films are strained due to epitaxial deposition on substrates with lattice mismatch. Perhaps, the most studied example is that of $BaTiO_3$ deposited on $SrTiO_3$ with a lattice mismatch of 2.2%, for which strain effects are expected in both polarization magnitude and ferroelectric transition temperatures. The strain mapping technique demonstrated here provides a method for direct measurement of epitaxial thin-film strains for correlation with, and enhancement of, such electrical properties. Strain mapping could also be used to assess strain inhomogeneity or relaxation arising from dislocation generation associated with minimizing elastic strain energy in films greater than a critical thickness, similar to that observed in SiGe films on Si substrates [33]. In another recent review, it was noted that domain walls rather than domains could be the active element in nanoelectronic applications and devices [44]. The importance of strain in determining both domain wall configuration and motion was noted, and EBSD strain mapping techniques, which can be extended down to near-10 nm spot sizes, can provide direct measurements for optimizing domain wall nanoelectronics. There is also the possibility of providing direct assessments of stress fields predicted from phase-field modeling of domain boundaries [45] and the effects of stress and strain on similar modeling of domain structure and boundary motion [46]. Finally, there is the exciting prospect of using strain mapping to develop flexoelectric devices [47, 48]. Such devices rely on the material property of polarization depending on strain *gradients*, and the results here make clear that strain gradients are easily measured for optimizing such materials.

Conclusions

High-resolution EBSD is an extremely effective measurement tool for quantitative determination of strain and thus stress in complicated micro- and nano-scale structures. The method was demonstrated here on a $BaTiO_3$ crystal containing bundles of *a*- and *c*- micro-domains separated by 90° domain boundaries. Orientation and strain maps with 2250 pixels and 0.2 μm × 0.5 μm pixel size were generated. Analysis of the strain maps showed strain variations within and between domains similar to those observed in larger, more geometrically regular domains, consistent with a loss of lattice tetragonality as an *a*–*c*-boundary was approached. The more complicated micro-domain structure led to a loss of plane-strain constraint such that significant shear strains existed in the bundles, distinct from the lamellae. Nonzero stress reference locations can be overcome by constructing stress maps from strain maps using separate imposed equilibrium conditions such that all stress components average to zero. Conditions for fracture in the structure can be calculated using a numerical integration scheme to determine a microstructural-based stress intensity factor from a stress map. Stable equilibrium spontaneous micro-crack lengths and conditions for crack instability under the action of a superposed applied stress can both be determined, with direct application to multi-layer ceramic capacitor reliability.

Acknowledgments

Certain commercial equipment, instruments, and software are identified in this paper in order to specify the experimental procedure adequately. Such identification is not intended to imply recommendation or endorsement by the National Institute of Standards and Technology, nor is it intended to imply that the equipment or software identified is necessarily best available for the purpose.

Electronic supplementary material: The online version of this article (doi:10.1007/s10853-017-1355-4) contains supplementary material, which is available to authorized users.

References

[1] Kishi H, Mizuno Y, Chazono H (2003) Base-metal electrode-multilayer ceramic capacitors: past, present and future perspectives. Jpn J Appl Phys Part 1(42):1–15

[2] Pan MJ, Randall CA (2010) A brief introduction to ceramic capacitors. IEEE Electr Insul Mag 26:44–50

[3] TDK Product Center, Multilayer Ceramic Chip Capacitors, https://product.tdk.com/info/en/products/capacitor/ceramic/mlcc/index.html. Accessed 8 Nov 2016

[4] Global and China Multi-layer Ceramic Capacitor (MLCC) Industry Report, 2015–2018. http://www.prnewswire.com/news-releases/global-and-china-multi-layer-ceramic-capacitor-mlcc-industry-report-2015-2018-300184096.html. Accessed 8 Nov 2016

[5] Davis C, Maloy S, and Wegman J (2000) Common cracking modes in surface mount multilayer ceramic capacitors. http://www.digikey.com/en/pdf/t/tdk/common-cracking-modes. Accessed 8 Nov 2016

[6] Chen K-Y, Huang C-W, Wu M, Wei W-CJ, Hsueh C-H (2014) Advanced characterization of mechanical properties of multilayer ceramic capacitors. J Mater Sci: Mater Electron 25:627–634

[7] den Toonder JM, Rademaker CW, Hu C-L (2003) Residual stresses in multilayer ceramic capacitors: measurement and computation. J Electronic Packaging 125:506–511

[8] Kwei GH, Lawson AC, Billinge SJL, Cheong SW (1993) Structures of the ferroelectric phases of barium-titanate. J Phys Chem 97:2368–2377

[9] Arlt G, Sasko P (1980) Domain configuration and equilibrium size of domains in $BaTiO_3$ ceramics. J Appl Phys 51:4956–4960

[10] Pramanick A, Jones JL, Tutncu G, Gjosh D, Stoica AD, An K (2012) Strain incompatibility and residual strains in ferroelectric single crystals. Sci Reports 2:929

[11] Howell JA, Vaudin MD, Cook RF (2014) Orientation, stress, and strain in an (001) barium titanate single crystal with 90° lamellar domains determined using electron backscatter diffraction. J Mater Sci 49:2213–2224

[12] Azough F, Al-Saffar R, Freer R (1998) A transmission electron microscope study of commercial X7R-type multilayer ceramic capacitors. J Eur Ceram Soc 18:751–758

[13] Forsbergh PW (1949) Domain structures and phase transitions in barium titanate. Phys Rev 76:1187–1201

[14] Merz WJ (1954) Domain formation and domain wall motions in ferroelectric in $BaTiO_3$ single crystals. Phys Rev 95:690–698

[15] Tsai F, Cowley JM (1992) Observation of ferroelectric domain boundaries in $BaTiO_3$ single crystals by reflection electron microscopy. Ultramicroscopy 45:43–53

[16] Park BM, Chung SJ, Kim HS, Si WM, Dudley M (1997) Synchrotron white-beam X-ray topography of ferroelectric domains in a BaTiO3 single crystal. Philos Mag A 75:611–620

[17] Rogan RC, Tamura N, Swift GA, Ustundag E (2003) Direct measurement of triaxial strain fields around ferroelectric domains using X-ray microdiffraction. Nature Mater 2:379–381

[18] Holt M, Hassani K, Sutton M (2005) Microstructure of ferroelectric domains in $BaTiO_3$ observed via X-ray microdiffraction. Phys Rev Lett 95:085504

[19] DeVries RC, Burke JE (1957) Microstructure of barium titanate ceramics. J Am Ceram Soc 40:200–206

[20] Burfoot JC (1959) A possible model for the switching of barium titanate crystals. Proc Phys Soc 73:641–649

[21] Bursill LA, Lin PJ (1984) Microdomains observed at the ferroelectric/paraelectric phase transition of barium titanate. Nature 311:550–552

[22] Jun C, Fan C-G, Qi L, Duan F (1988) Transmission electron microscope studies of para-ferroelectric transitions in $BaTiO_3$ and $KNbO_3$. J Phys C: Solid State Phys 21:2255–2266

[23] Park BM, Chung SJ (1994) Optical, electron microscopic, and X-ray topographic studies of ferroic domains in barium titanate crystals grown from high-temperature solution. J Am Ceram Soc 77:3193–3201

[24] Cheng S-Y, Ho N-J, Lu H-Y (2006) Transformation-induced twinning: the 90° and 180° ferroelectric domains in tetragonal barium titanate. J Am Ceram Soc 89:2177–2187

[25] Mase WE (1970) Continuum Mechanics. McGraw-Hill, New York

[26] Nye JF (1979) Physical Properties of Crystals their representation by tensors and matrices. Oxford University Press, Oxford

[27] Berlincourt D, Jaffe H (1958) Elastic and piezoelectric coefficients of single-crystal barium titanate. Phys Rev 111:143–148

[28] Wilkinson AJ, Meaden G, Dingley DJ (2006) High resolution mapping of strains and rotations using electron backscatter diffraction. Mater Sci Technol 22:1271–1278

[29] Vaudin MD, Gerbig TB, Stranick SJ, Cook RF (2008) Comparison of nanoscale measurements of strain and stress using electron back scattered diffraction and confocal Raman microscopy. Appl Phys Let 93:193116

[30] Vaudin MD, Stan G, Gerbig YB, Cook RF (2011) High resolution surface morphology measurements using EBSD cross-correlation techniques and AFM. Ultramicroscopy 111:1206–1213

[31] Friedman LH, Vaudin MD, Stranick SJ, Stan G, Gerbig YB, Osborn WA, Cook RF (2016) Assessing strain mapping by

electron backscatter diffraction and confocal Raman microscopy using wedge-indented Si. Ultramicroscopy 163:75–86

[32] Wilkinson AJ (2006) High resolution measurements of strain and tilt distributions in SiGe mesas using electron backscatter diffraction. Appl Phys Let 89:241910

[33] Vaudin MD, Osborn WA, Friedman LH, Gorham JM, Cook RF (2015) Designing a standard for strain mapping: HR-EBSD analysis of SiGe thin film structures on Si. Ultramicroscopy 148:94–104

[34] Lawn BR (1993) Fracture of Brittle Solids-Second Edition. Cambridge University Press, Cambridge

[35] Michaels CA, Cook RF (2016) Determination of residual stress distributions in polycrystalline alumina using fluorescence microscopy. Mater Design 107:478–490

[36] Cook RF, Fairbanks CJ, Lawn BR, Mai Y-W (1987) Crack resistance by interfacial bridging: its role in determining strength characteristics. J Mat Res 2:345–356

[37] deWith G (1993) Structural Integrity of ceramic multilayer capacitor materials and ceramic multilayer capacitors. J Eur Ceram Soc 12:323–336

[38] Rattanachan S, Miyashita Y, Mutoh Y (2005) Fracture toughness of $BaTiO_3$ and $BaTiO_3$-Al_2O_3 composite under electric field. In: Bradt RC, Munz D, Sakai M, White KW (eds) Fracture Mechanics of Ceramics. Springer, New York, pp 297–305

[39] Galal Yousef S, Rödel J, Fuller ER Jr, Zimmermann A, El-Dasher BS (2005) Microcrack evolution in alumina ceramics: experiment and simulation. J Am Ceram Soc 88:2809–2816

[40] Yoneda Y, Kohmura Y, Suzuki Y, Hamazaki S, Takashige M (2004) X-ray diffraction topography on a $BaTiO_3$ crystal. J Phys Soc Jpn 73:1050–1053

[41] Dennis MD, Bradt RC (1974) Thickness of 90 degrees ferroelectric domain walls in (Ba, Pb)TiO3 single crystals. J Appl Phys 45:1931–1933

[42] Zhang X, Hashimoto T, Joy DC (1992) Electron holographic study of ferroelectric domain walls. Appl Phys Let 60:784–786

[43] Dawber M, Rabe KM, Scott JF (2005) Physics of thin-film ferroelectric oxides. Rev Modern Phys 77:1083–1130

[44] Catalan G, Seidel J, Ramesh R, Scott JF (2012) Domain wall nanoelectronics. Rev Modern Phys 85:119–156

[45] Su Y, Landis CM (2007) Continuum thermodynamics of ferroelectric domain evolution: theory, finite element implementation, and application to domain wall pinning. J Mech Phys Solids 55:280–305

[46] Woldman AY, Landis CM (2016) Phase-field modeling of ferroelectric to paraelectric phase boundary structures in single-crystal barium titanate. Smart Mater 25:035033

[47] Ma W, Cross LE (2006) Flexoelectricity of barium titanate. Appl Phys Let 88:232902

[48] Zubko P, Catalan G, Tagantsev AK (2013) Flexoelectric effect in solids. Ann Rev Mater Res 43:387–421